

# Local Stability Analysis and Eigenvalue Sensitivity of Reacting, Bluff Body Wakes

Benjamin Emerson<sup>1</sup>†, Tim Lieuwen<sup>1</sup>  
and Matthew P. Juniper<sup>2</sup>

<sup>1</sup>Ben T. Zinn Combustion Lab, Department of Aerospace Engineering, Georgia Institute of Technology, 635 Strong Street, Atlanta, GA 30318, USA

<sup>2</sup>Department of Engineering, University of Cambridge, Trumpington Street, Cambridge CB2 1PZ, U.K.

(Received ?; revised ?; accepted ?. - To be entered by editorial office)

This paper presents an experimental and theoretical investigation of high Reynolds number, low density reacting wakes near a hydrodynamic Hopf bifurcation. This configuration is applicable to the wake flows that are commonly used to stabilize flames in high velocity flows. First, an experimental study is conducted to measure the limit cycle oscillation of this reacting bluff body wake. The experiment is repeated while independently varying the bluff body lip velocity and the density ratio across the flame. In all cases, the wake exhibits a sinuous oscillation. Linear stability analysis is performed on the measured time-averaged velocity and density fields. In the first stage of this analysis, a local, spatio-temporal stability analysis is performed on the measured, time averaged velocity and density fields. The stability analysis results are compared to the experimental measurement, and demonstrate that the local stability analysis correctly captures the influence of the lip velocity and density ratio parameters on the sinuous mode. In the second stage of this analysis, the linear direct and adjoint global modes are estimated by combining the local results. The sensitivity of the eigenvalue to changes in intrinsic feedback mechanisms is found by combining the direct and adjoint global modes. This is referred to as the eigenvalue sensitivity throughout the paper for reasons of brevity. The predicted global mode frequency is consistently within 10 % of the measured value, and the linear global mode shape closely resembles the measured nonlinear oscillations. The adjoint global mode reveals that the oscillation is strongly sensitive to open loop forcing in the shear layers. The eigenvalue sensitivity identifies a wavemaker in the recirculation zone of the wake. A parametric study shows that these regions change little when the density ratio and lip velocity change. In the third stage of the analysis, the stability analysis is repeated for the varicose hydrodynamic mode. Although not physically observed in this unforced flow, the varicose mode can lock into longitudinal acoustic waves and cause thermoacoustic oscillations to occur. This paper shows that the local stability analysis successfully predicts the global hydrodynamic stability characteristics of this flow and shows that experimental data can be post-processed with this method in order to identify the wavemaker regions and the regions that are most sensitive to external forcing, for example from acoustic waves.

**Key words:** Keyword 1, Keyword 2...

---

† Email address for correspondence: bemerson@gatech.edu

## 1. Introduction

### 1.1. Motivation

The bluff body combustor is prevalent in industrial and aerospace applications, and serves as a canonical burner for many fundamental combustor studies. Fluid dynamics plays an integral role in the operability of bluff body combustors. For example, the turbulent and coherent structures that stem from hydrodynamic instabilities govern important combustor phenomena such as mixing, entrainment, blowout (Shanbhogue *et al.* 2009), and combustion instability (O'Connor & Lieuwen 2011; Smith & Zukoski 1985; Poinso *et al.* 1987; Soteriou & Ghoniem 1994). Bluff body combustors are especially prone to combustion instability, which plagues the combustion communities of both the energy and aerospace industries (Zinn & Lieuwen 2005).

Combustion instability is the resonant coupling between the acoustics of the combustor and the unsteady heat release of combustion. This is typically an unwanted phenomenon, which can cause severe damage to hardware, problems with excessive heat transfer, and even blowout of the flame from the combustor. The challenges associated with understanding and predicting combustion instabilities lie in the flame response to the acoustic field. One of the most complicated flame response mechanisms is the velocity coupled flame response, where the flame responds dynamically not only to the acoustic velocity, but also to the vortically induced velocity field excited by the acoustics (Lieuwen 2012). This vortically induced, or hydrodynamic, velocity field holds critical importance for the flame response but is typically computationally expensive to predict, especially over the broad operability map of the combustor. Local stability analysis applied around a mean flow, which could, for instance, be obtained inexpensively from a RANS solver, offers an inexpensive alternative to traditional computational approaches. With this in mind, this study explores the capability of local stability analysis, applied around a mean flow, to quantify the hydrodynamic stability of bluff body combustors, and to identify the regions of the flow in which hydrodynamic oscillations are expected to couple most strongly with acoustic oscillations.

### 1.2. Background

The high Reynolds number, uniform density wake behind a bluff body generally exhibits the globally unstable, sinuous Von Karman vortex street. This wake instability can be influenced by suction/blowing (Fransson *et al.* 2004), trailing splitter plates (Cardell 1993), wake heating (Roshko 1954; Zdravkovich 1997; Yu & Monkewitz 1990; Soteriou & Ghoniem 1994), and numerous other modifications. Strykowski & Sreenivasan (1990) showed that the oscillations of this global mode can be suppressed by adding a small control cylinder downstream and to one side of the wake. Hill (1992) and Giannetti & Luchini (2007) identified this region by calculating the direct and adjoint global modes of the steady but unstable flow behind a cylinder at  $Re \sim 50$ . They overlapped these to obtain the sensitivity of the eigenvalue to changes in intrinsic feedback mechanisms, referred to throughout the paper as the 'eigenvalue sensitivity' for reasons of brevity. The eigenvalue sensitivity reveals the region of the flow in which changes to the stability operator, e.g. by passive feedback, cause the biggest eigenvalue drift. This region is known as the wavemaker region of the flow, in that oscillations are generated in this region and the rest of the flow merely responds to these oscillations. This analysis was subsequently refined by Luchini *et al.* (2009) and Marquet *et al.* (2008) in order to include the influence that the control cylinder has on the base flow. These techniques predict the region in which the control cylinder most stabilizes the flow and identifies the corresponding stabilization mechanism.

In this paper, we examine a confined bluff body wake flow. Lateral confinement can have substantial influences on absolute stability of the wake (Juniper & Candel 2003). This becomes significant when the confinement ratio,  $h$ , defined as the width of the outer flow divided by the half-width of the inner flow, is below 4. Confined high density wakes are particularly absolutely unstable and this effect is strongest when  $h = 1$  (figure 16 of Juniper (2006)). Rees & Juniper (2010) show that confinement is destabilizing in viscous planar wakes but that the destabilizing influence of confinement starts to diminish below  $Re = 1000$ . In this study we consider the effect of the confining walls because the confinement ratio is  $h = 0.3$  and the Reynolds number is well above  $Re = 1000$  (ranging from  $Re = 10,000$  to  $Re = 27,000$  over the conditions tested).

Bluff body flame stabilization is used often in aerospace and duct heating applications. In the reacting wake of a bluff body stabilized flame, combustion causes a spatially non-uniform mean density field with a lower density in the wake. A variety of prior studies has noted fundamental differences in the dynamic character of the flame and flow field at different levels of preheat, and consequently different flame density ratios (Erickson *et al.* 2006; Kiel *et al.* 2006; Cross *et al.* 2010; Emerson *et al.* 2012). The first systematic demonstration showing the effects of flame density ratio in combustor flows was presented by Erickson *et al.* (2006). Their results show that sinuous vortex shedding is suppressed at high flame density ratios, but that a large sinuous flow feature gradually grows in prominence as the density ratio across the flame is decreased below values of approximately 2-3. Compared to a uniform density wake, non-uniform density alters the stability of the flow through the action of baroclinic torque (Meliga *et al.* 2008; Lesshafft & Huerre 2007). Using simple models, Yu & Monkewitz (1990) express the density non-uniformity as a density ratio. They demonstrate the effect of the density ratio parameter, showing that dense wakes are more absolutely unstable than low density wakes. Wakes with sufficiently low density relative to the outer flow are globally stable, and only convectively unstable. In this paper we do not rely on the model results in Yu & Monkewitz (1990), which utilize piece-wise linear velocity/density profiles. Instead, we calculate the absolute growth rate of experimentally measured time-averaged velocity and density profiles. The velocity fields are measured with particle image velocimetry (PIV), and the density fields are estimated from the Mie scattering images acquired for the PIV measurement. For the moderate density ratios in this study, we find that the flows have a region of absolute instability, even though they are low density wakes. For these wakes, the sinuous mode is hydrodynamically more globally unstable than the varicose mode, so the sinuous mode dominates when there is no external forcing.

Combustors utilizing reacting bluff body wakes typically have a stream-wise dimension that is longer than their cross-stream dimensions, so the lowest frequency acoustic mode is longitudinal. A longitudinal acoustic wave forces the bluff body wake in a varicose manner. Although the bluff body wake is more hydrodynamically unstable to sinuous motions, it is also convectively unstable to varicose motions. It amplifies these and causes heat release oscillations in time with the acoustic oscillations. If these heat release oscillations are sufficiently in phase with the pressure oscillations then these thermoacoustic oscillations become self-sustained. Experiments show that the varicose mode seems to be especially troublesome for thermoacoustic oscillations (Emerson *et al.* 2013). The local analysis used in this study can find the direct and adjoint global modes for the varicose motion in the same way as they can for the sinuous motion, even when the flow is not globally unstable. This is difficult with global analyses, which are strongly influenced by the downstream boundary condition when the flow is not globally unstable (Garnaud *et al.* 2013).

The above studies demonstrate that low density ratio, reacting bluff body wakes os-

cillate sinusoidally in the absence of acoustic forcing or thermoacoustic oscillations. Experimental studies on low Reynolds number, uniform-density wakes show that these oscillations are driven by a wavemaker region just behind the bluff body. The goal of this paper is to answer three questions. The first question is whether or not local stability analysis is an appropriate tool for studying the hydrodynamics of high  $Re$ , low density wakes. The second question is whether we can use direct/adjoint techniques to identify the wavemaker region of our experimentally measured reacting bluff body wake in the sinuous and the varicose regimes. The third question is what influence, if any, do the lip velocity and density ratio have on the wavemaker and the region of high receptivity to velocity forcing.

## 2. Local Hydrodynamic Stability Analysis

The goals outlined at the end of section 1 are accomplished by performing a local stability analysis around an experimentally-derived time-averaged base flow at high Reynolds number. It is important to note that this analysis is local-only, and that the global modes presented in this paper are estimated by combining the local results. The procedure for combining the local results is outlined later in this section. The use of a base flow that is time-averaged, rather than a steady solution to the Navier–Stokes equations, will be discussed in section 5.

A local stability analysis has two advantages over a 2D global stability analysis. Firstly, the streamwise domain of the experimental data is shorter than the length of the direct global mode. It is significantly shorter than that in figure 19 of Giannetti & Luchini (2007), which shows the influence of the downstream boundary. This presents a challenge for a 2D global stability analysis because the boundaries lie in regions in which the direct and adjoint global modes have significant amplitude. This means that boundary conditions at the upstream and downstream ends of the domain need to be carefully chosen. This is a challenge that faces the global analysis approach, although it is not an insurmountable problem. On the other hand, in a local analysis, slices of the flow at each streamwise location are considered independently, which means that no streamwise boundary conditions need to be imposed. The removal of upstream and downstream boundary conditions is a convenience of the local analysis compared to a global scheme. Secondly, 2D global stability analysis is much more computationally expensive than a local analysis. For these reasons, we use a local stability analysis, as in Juniper & Pier (2015), to reconstruct the direct and adjoint global modes.

In a local analysis, the wavelength of the perturbations is assumed to be much shorter than the length scale over which the base flow varies (the WKBJ approximation). This approximation is valid for flows that are nearly parallel, but it also works surprisingly well for flows that are significantly non-parallel (Pier 2008). The motivations for using the WKBJ approximation parallel those for using a local analysis, discussed in the previous paragraph. The justification for using this approach is that it is robust for weakly non-parallel flows like those considered in this analysis. Additionally, as opposed to a fully global approach, this approach also precludes acoustic feedback, which is a benefit for isolating hydrodynamic instabilities.

The governing equations are Navier–Stokes equations, linearized around a parallel base flow that is symmetric about the flow centreline. Equations 2.1, 2.2, and 2.3 show the governing equations, where  $x$  and  $y$  are the streamwise and transverse directions, and  $U_0$  and  $\rho_0$  are the base axial velocity and density. Also,  $u$ ,  $v$ , and  $p$  are the transverse dependence of the linear perturbations to the axial velocity, transverse velocity, and pressure, which take the general form  $p(y)e^{-i\omega t}e^{ikx}$  (for the pressure, for example).

$$iku(y) + \frac{dv}{dy} = 0 \quad (2.1)$$

$$-i\omega\rho_0(y)u(y) + ikU_0(y)\rho_0(y)u(y) + \rho_0(y)\frac{dU_0}{dy}v(y) = -ikp(y) + \frac{1}{Re}(-k^2u(y) + \frac{d^2u}{dy^2}) \quad (2.2)$$

$$-i\omega\rho_0(y)v(y) + ikU_0(y)\rho_0(y)v(y) = -\frac{dp}{dy} + \frac{1}{Re}(-k^2v(y) + \frac{d^2v}{dy^2}) \quad (2.3)$$

The base flow includes the spatially-varying base density field. This approach captures instabilities generated by the Kelvin-Helmholtz mechanism, which is influenced by the base-density nonuniformity, although it does not capture the Darrieus-Landau instability, the inclusion of which is left to future work. The boundary conditions are no slip and impermeability at the confining wall, and sinuous or varicose modes at the flow centreline. A Fourier/Laplace decomposition is performed in time and in the  $x$ -direction such that the governing equations reduce to an eigenvalue problem that is only satisfied for certain eigenvalue pairs of the streamwise wavenumber,  $k$ , and the angular frequency,  $\omega$  (Huerre & Monkewitz 1990, 2000). The stages of the local analysis are described in detail in Juniper *et al.* (2011), and are summarised next.

Stage 1 of the local analysis is to evaluate the absolute growth rate,  $\omega_0$ , as a function of downstream distance,  $x$ . The absolute growth rate is the growth rate of waves with zero group velocity at that streamwise location. These waves satisfy  $d\omega/dk = 0$ . Stage 2 of the local analysis is to evaluate the linear global mode frequency,  $\omega_g$ , and the wave maker location. Stage 3 of the local analysis is to force the flow at  $\omega_g$  and to evaluate the spatial growth rates of the downstream-travelling wave,  $k^+$ , and the upstream-travelling wave,  $k^-$ . These can then be combined to form the direct global mode and the adjoint global mode (Juniper & Pier 2015; Juniper *et al.* 2011). In this analysis, we do not develop non-parallelism, and we do not solve an equation for the slowly-varying amplitude.

Stages 1-3 of the analysis proceed as follows. In stage 1, the local stability analysis is performed with the software package InstaFlow, described in Juniper (2012) and Juniper *et al.* (2011). At each streamwise location, the time-averaged streamwise velocity,  $U(y)$ , and time-averaged density,  $\rho(y)$ , are projected onto Gauss-Lobatto-spaced points in the cross stream,  $y$ , direction. The Gauss-Lobatto grid consists of 60 grid points spanning half of the channel from the centerline to the wall. A grid independence study showed that this grid provided better than 0.12 % error in the Eigenvalue. The governing equations and boundary conditions are expressed in matrix form using Chebyshev differentiation matrices. At each slice, this generates a matrix eigenvalue problem for  $\omega$  in terms of  $k$ . Saddle points of  $\omega(k)$  are found and their Briggs-Bers validity is checked. These saddle points are then tracked as the streamwise location changes. For these flows, there is usually only one valid saddle point for sinuous oscillations and another valid saddle point for varicose oscillations. In stage 2, the linear global mode frequency is calculated by fitting a 7<sup>th</sup> order Padé polynomial to  $\omega_0(x)$  and finding the saddle position in the complex  $(X, \omega_0)$ -plane (Juniper & Pier 2015), denoted  $(x_g, \omega_g)$ . The dependence of  $x_g$  and  $\omega_g$  on the polynomial order is shown in Figure 1. In stage 3 of the analysis, each of the local analyses (at each axial position) is repeated, this time solving for  $k$  when  $\omega = \omega_g$ . For a given value of  $\omega$ , there are two valid solutions to  $k$ , which are the  $k^+$  and  $k^-$  spatial branches. These  $k^+$  and  $k^-$  branches are conveniently identified at  $x_g$ , where they are singular. The  $k^+$  branch is the more spatially amplified branch when moving in the downstream direction, and is numerically tracked while walking downstream from  $x_g$ ,

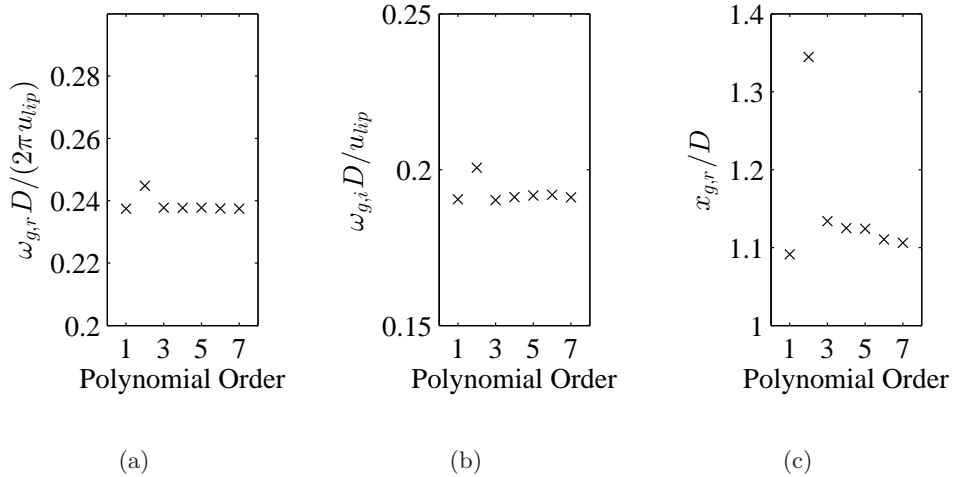


FIGURE 1. Dependence of  $\omega_g$  and  $x_g$  on the Padé polynomial order, showing a) real part of  $\omega_g$  nondimensionalized as the Strouhal number, b) imaginary part of  $\omega_g$ , and c)  $x_{g,r}$ , shown for a representative case ( $\rho_u/\rho_b = 1.7$ ,  $U_{tip} = 30$  m/s)

while the  $k^-$  branch is the more spatially amplified branch when moving in the upstream direction and is numerically tracked while walking upstream of  $x_g$ . At each stage, the Eigenfunctions are normalized to have  $u^2 + v^2 + p^2 = 1$

### 3. Design of Experiments

The goal of the experiments is to obtain estimates of base flows for stability analysis, and to measure the corresponding global mode frequencies and mode shapes. The facility and its instrumentation are described in detail in the next subsection. Its test section is a nominally two-dimensional bluff body combustor with premixed inflow; therefore, the base flow is a planar wake with spatially varying density, confined within a channel. Three different streams are premixed upstream of the test section: room temperature natural gas, room temperature air, and a vitiated stream. The vitiated stream consists of hot combustion products from a natural gas pre-burner. Independent control of these three streams provides significant flexibility of the flame density ratio and the bluff body lip velocity in the test section. This is significant, because the flame density ratio controls the global mode growthrate,  $\omega_{g,i}$ , and the lip velocity governs the global mode frequency,  $\omega_{g,r}$ , in the linear analysis. The test matrix, discussed in section 3.3, is constructed to vary these parameters.

#### 3.1. Experimental Facility

The experimental rig, shown in Figure 2 and Figure 3, consists of two premixed, methane-air combustors in series. The first combustor is used to vitiate the flow and raise its temperature. The second, bluff body stabilized combustor consists of a rectangular section with a bluff body spanning the width of the combustor, creating a nominally 2D flow. The bluff body has a diameter of  $D = 19.1$  mm. The aspect ratio of bluff body height to chamber width is 0.15. This combustor has quartz windows for optical access from all four sides. The bluff body used in the test section, shown in Figure 3b has a 2D ballistic

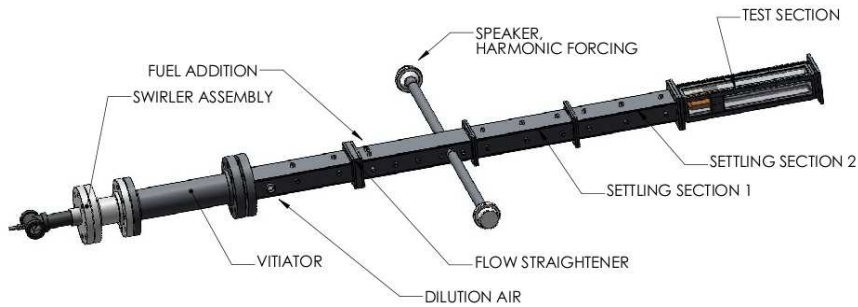


FIGURE 2. Schematic of the atmospheric pressure, vitiated, bluff body rig

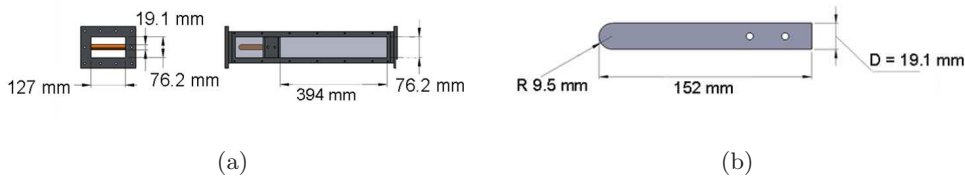


FIGURE 3. Drawings of a) the test section and b) the bluff body

shape. Additional fuel and air injection sources are located between the two burners, allowing substantial flexibility in density ratio and lip velocity. The Reynolds number for these experiments varies from  $Re = 10,000$  to  $Re = 27,000$ . Further details of this facility and its design are provided in Emerson *et al.* (2012).

### 3.2. Diagnostics

Velocity fields are measured using particle image velocimetry (PIV). Mie scattering images for high speed PIV are obtained as follows. The flow is seeded with  $5 \mu\text{m}$   $\text{Al}_2\text{O}_3$  particles, chosen due to their durability in reacting flows and their high refractive index (Melling 1997). This particle size is chosen because it is large enough to slow down accumulation on and clouding of the test section windows, while retaining a sufficiently small Stokes number to accurately track the flow at the frequencies of interest. Following the work by Mei (1996), the Stokes number calculated for this flow and seed particle combination is 0.015. This Stokes number is calculated using a kinematic viscosity of  $3 \times 10^{-4} \text{ m}^2/\text{s}$ , and oscillation frequency of 850 Hz (roughly the highest global mode frequency encountered). This Stokes number is comfortably below the cutoff Stokes number for solid particles in air (Mei 1996), which is in the range of .02-.04 and would correspond to a frequency of at least 1500 Hz.

The particle-laden flow is illuminated with a double-pulsed Nd:YLF laser, with wavelength of 527 nm, pulse duration of 100 ns, and 4 mJ/pulse pulse energy. Each of the two lasers in the double-pulsed system is operated at 5000 Hz. The laser beams are expanded with a -50 mm cylindrical lens into an expanding sheet, and the sheet is shaped with a 750 mm cylindrical lens to have a nominally 4 mm thickness. An expanding sheet is chosen instead of a collimated sheet because of the large test area. The time-delay,  $dt$ , between the two illuminating laser pulses of a given pair was  $12 \mu\text{s}$ . The short  $dt$  is responsible for much of the velocity uncertainty, as discussed below. Mie scattering image pairs are captured by a high speed CMOS camera with  $20 \mu\text{m}$  pixels. The camera is outfitted with a 55 mm lens, with aperture at f/5.6. The camera is operated with a pixel resolution of

640 × 448, with image pairs acquired at a frame rate of 5 kHz. The optical configuration produces a magnification of 1:12.5, such that the measurement domain covers a 640 × 320 pixel region of the CMOS chip, which corresponds to a region of the combustor that is roughly 160 mm long in the axial direction and 80 mm wide in the transverse direction. The measurement plane is located at the center-span of the bluff body. The diffraction limited spot size for this configuration is 7 μm. Slight defocusing, together with the natural aberration and imperfections of the imaging optics, distributes the scattered light from the particles over a nominal 3 pixel diameter. A bandpass optical filter is placed in front of the camera in order to reject the majority of flame and other background luminosity. The filter pass-band is centered at 527 nm and has a transmission of greater than 93 % from 517 nm to 537 nm.

Velocity vectors are computed from the Mie scattering image pairs using a digital cross-correlation algorithm (Willert 1991) with a multi-pass approach (Soria 1996) and 2D Gaussian sub-pixel interpolation (Willert 1991). The multi-pass analysis consists of a single pass with 64 × 64 pixel interrogation windows and 50 % overlap between interrogation windows, followed by 2 passes with 32 × 32 pixel interrogation windows and 50 % overlap between the interrogation windows. The spacing between vectors is 4 mm.

Post-processing algorithms are used to discard and replace a small number of spurious vectors, and to validate the PIV data. First, any velocity vector with an axial component outside of a 20 m/s ± 90 m/s range or a transverse component outside of a ± 45 m/s range is discarded. These ranges are based on the expected range of mean axial and transverse velocities, and additionally, they conservatively accommodate coherent structures with unsteady velocity on the order of the nominal 50 m/s lip velocity. Next, any velocity vector whose velocimetry calculation has a peak correlation coefficient less than 0.2 is discarded and a local validation method discards neighboring vectors whose ratio of difference to average velocity magnitude is greater than 20 % of the rms of the nearest neighbors. This threshold is consistent with values recommended in the literature (J. Nogueira 1997). In all, less than 1 % of the total velocity vectors are discarded and their values filled with the instantaneous average of neighboring vectors.

The PIV measurement is calibrated by imaging a black anodized aluminum calibration plate with a laser etched pattern, which is located coincidentally with the laser light sheet. The laser etched pattern consists of a regularly spaced grid of crosses, composed of 0.3 mm thick lines, with spacing of 6 mm and with positional uncertainty of .004 %. The spatial coordinates of the Mie scattering images and resultant velocity fields are mapped to this grid. The worst-case calibration error is estimated to be 1 pixel over the large 160 mm calibration plate, which would result in a small 0.2 % bias error. The phase jitter between the pair of laser illumination pulses is measured to be on the order of nanoseconds, which is significantly less than the relatively long 100 ns duration at half-maximum of each illumination. Therefore, the duration of the laser illumination dominates the temporal measurement uncertainty, which is less than 1 % of the time delay between the pair of illumination pulses. Peak-locking during sub-pixel interpolation (Fincham & Spedding 1997), combined with the relatively short  $dt$ , is estimated to provide a velocity uncertainty of 4 %. In/out of plane motion dominates the random velocity uncertainty over much of the measurement domain, and increases with distance from the measurement center (located at  $x/D = 4$ ). For example, at axial positions 20 mm from the measurement center (ie at  $x/D = 3$  and  $x/D = 5$ ), this uncertainty is 5 %. As the measurement position moves to the extreme axial extents of the measurement, ie to  $x/D = 0$  and  $x/D = 8$ , this uncertainty increases linearly to 20 %. However, this uncertainty due to in and out of plane motion applies to turbulence and secondary instabilities in this flow, but does not directly impact the nominally 2D hydrodynamic motion and time averaged



velocity field of interest. Just downstream of the bluff body, from  $x/D = 0$  to  $x/D = 0.3$ , laser light scattering off of the bluff body spoils the PIV measurement and introduces large uncertainties; we do not report results from this region.

The measured oscillatory velocity magnitude is subject to an additional source of uncertainty. Following the seeding particle Stokes number discussion above, the seeding particles are expected to respond at the forcing frequency with 92 % of the flow response amplitude, and with less than a 20 degree phase delay. It is important to note that the significant experimental velocity field uncertainties lie in the unstead velocity magnitude. The uncertainty in the measured oscillatory velocity affects the validation of the stability analysis, and is quantified with error bars when compared to stability analysis predictions. The time-averaged velocity, which is used as an input to the stability analysis, is not subject to these larger experimental uncertainties.

The time-averaged density field is estimated from the Mie scattering images. An edge detection algorithm is used to extract the sharp jump in seed particle density that occurs at the flame sheet (Gülder *et al.* 2000). The instantaneous density is then specified as a binary field having either the burned or unburned value. The unburned density value is estimated from a temperature measurement just upstream of the test section, and a gas composition consisting of the vitiated gas stream mixed with the fresh air and fuel streams. The burned density value is estimated as the adiabatic flame temperature of this mixture. The instantaneous density fields are then averaged at each location to obtain the temporally averaged density field. The key assumption behind this method is that the density change occurs across a thin, unbroken reaction zone, such that there is minimal turbulent mixing between reactants and products outside of this thin zone. This assumption is supported by the modified Borghi-Peters diagram (Peters 1999), due to two considerations for this flow. The first consideration is that the laminar flame thickness is very thin relative to the bluff body diameter, which is well satisfied for this problem, as verified by detailed chemical kinetic calculations of an unstretched, premixed flame (using GRI 3.0) showing that the estimated flame thickness is roughly 2 % of the bluff-body diameter (and hence the integral length scale). The second consideration is that the turbulence intensity is less than 50 times the laminar flame speed. We quantified the uncertainty of this density ratio measure in a previous study, and demonstrated that it is better than 10 % (Emerson 2013), which is less than the step-changes in density ratio reported here during density ratio sweeps.

### 3.3. Test Matrix Design

The test matrix is designed to vary the global mode growth rate and frequency. This is accomplished by sweeping two stability parameters: the density ratio and the lip velocity. Previous studies have shown that the absolute growthrate is sensitive to the density ratio (Yu & Monkewitz 1990), and that the global mode frequency scales with the bluff body lip velocity,  $f_g = St_D U_{lip} / D$  (Prasad & Williamson 1997). In these experiments, the density ratio is varied over the range of  $\rho_u / \rho_b = 1.7$  to  $\rho_u / \rho_b = 2.5$  to sweep the global mode growthrate. For each density ratio, the bluff body lip velocity is varied from 20 m/s to 70 m/s in order to vary the global mode frequency. The Reynolds number for these experiments ranges from  $Re = 10,000$  to  $Re = 27,000$ .

The experimental parameters, bluff body lip velocity  $U_{lip}$  and density ratio  $\rho_u / \rho_b$ , are determined as follows. The bluff body lip velocity is calculated as  $U_{lip} = \dot{m} / (\rho_u A_{lip})$ , which is an average streamwise flow velocity. The mass flowrate,  $\dot{m}$ , is the mass flowrate entering the test section. The area,  $A_{lip}$ , is the cross-sectional area of the flow at the plane of the bluff body trailing edge, accounting for the blockage of the bluff body. The density of the wake, which consists of burned products, is denoted  $\rho_b$ , and the density of

the unburned flow outside of the wake is denoted  $\rho_u$ . The values of these densities are estimated according to the procedure outlined at the end of Section 3.2.

## 4. Experimental Results

### 4.1. Base Flow Approximation

This section describes the experimentally-measured mean flow field, which is the base flow used for the stability analysis. The time averaged axial velocity field is plotted in Figure 4a. This plot shows that the velocity profile is that of a recirculating wake. The reverse flow in the recirculation zone reaches a maximum reverse flow velocity between 1 and 2 bluff body diameters downstream, which is generally true for all conditions tested in this study. Figure 4b plots the time averaged density field generated by the bluff-body stabilized flame. This plot shows that the mean density field consists of a region of low density flow (hot combustion products) in the wake region, and high density flow (reactants) in the free-stream. The density field also illustrates that this flow holds a nearly flat flame, which 'pinches' slightly just downstream of the recirculation zone. The small spreading angle of the flame is due to the fact that the free stream velocity is two orders of magnitude faster than the laminar flame speed.

### 4.2. Flow Dynamics

Figure 5 shows power spectra of the unsteady transverse velocity at three different density ratios and velocities. Figure 5a presents power spectra for three values of  $\rho_u/\rho_b$ , and shows that there is a strong narrowband peak at  $St_D = 0.24$ . The frequency of this response is proportional to the bluff body lip velocity, as is evident in Figure 5b. This indicates that the strong oscillation is driven by a hydrodynamic mechanism, not an acoustic mechanism.

The global mode associated with the  $St_D = 0.24$  oscillations is sinuous, as it is for a non-reacting wake. To illustrate this, we perform a Proper Orthogonal Decomposition (POD) on the velocity field (Berkooz *et al.* 1993). The POD decomposes the velocity field,  $\vec{u}(\vec{x}, t)$  into a series of  $N$  spatial basis functions,  $\phi_n(\vec{x})$ , each with temporal evolution of  $q_n(t)$ , such that

$$\vec{u}(\vec{x}, t) = \sum_{n=1}^N q_n(t) \phi_n(\vec{x}) \quad (4.1)$$

Here,  $\vec{x}$  is a spatial position vector that points to the axial position,  $x$ , and transverse position,  $y$ . Figure 6 shows the most energetic pair of POD modes along with the corresponding spectra of their time coefficients. This pair of POD modes is selected because the two modes combine to reconstruct the global mode (Ma *et al.* 2000; Perrin *et al.* 2007; Konstantinidis *et al.* 2007). The time coefficients for each POD mode are denoted  $q_n$  and their power spectral densities are denoted  $|q_n|^2$ , where  $n$  is the number of the POD mode. Together, these two modes represent a strong sinuous vortex shedding at the  $St_D = 0.24$  frequency. A detailed discussion of the dynamics of this flow is provided by Emerson *et al.* (2012) and Emerson (2013).

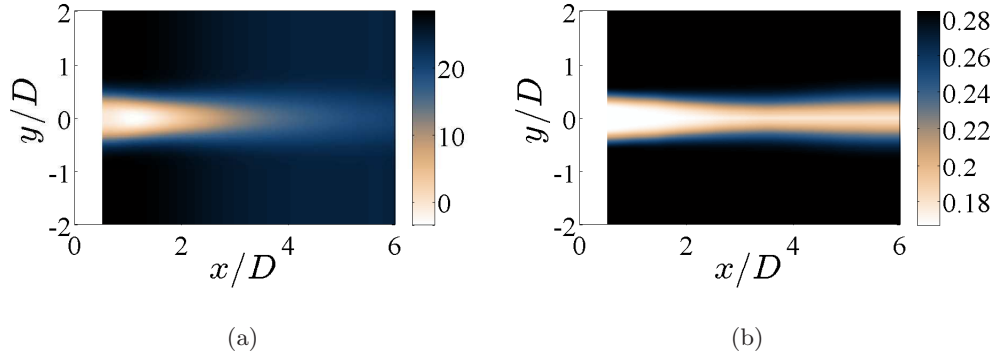


FIGURE 4. Contour plots of the measured base flow, showing a) axial velocity field, and b) density field. Conditions are  $\rho_u/\rho_b = 1.7$ ,  $U_{tip} = 30$  m/s, which are qualitatively representative of all cases.

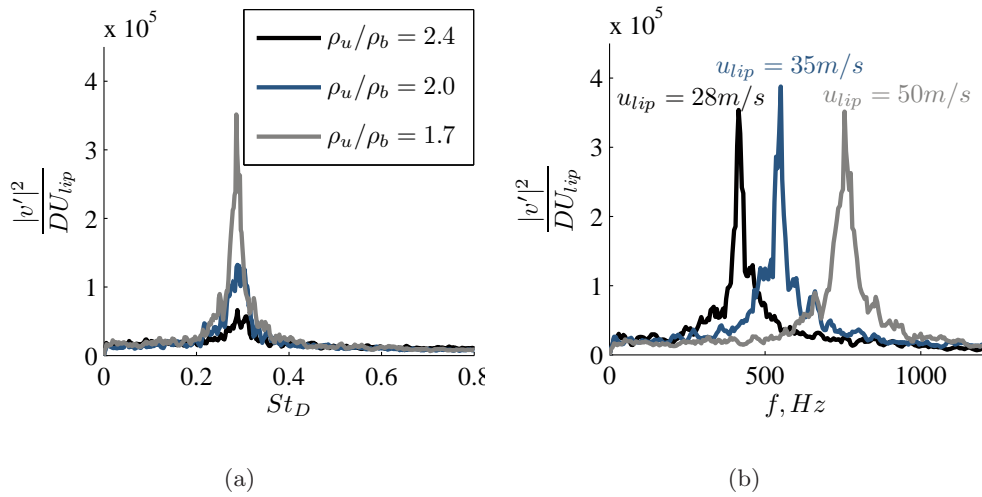


FIGURE 5. Power spectra of the centerline transverse velocity at  $x/D = 5$ ,  $y/D = 0$ , for a) three density ratios at  $U_{tip} = 50$  m/s and b) three velocities at  $\rho_u/\rho_b = 1.7$

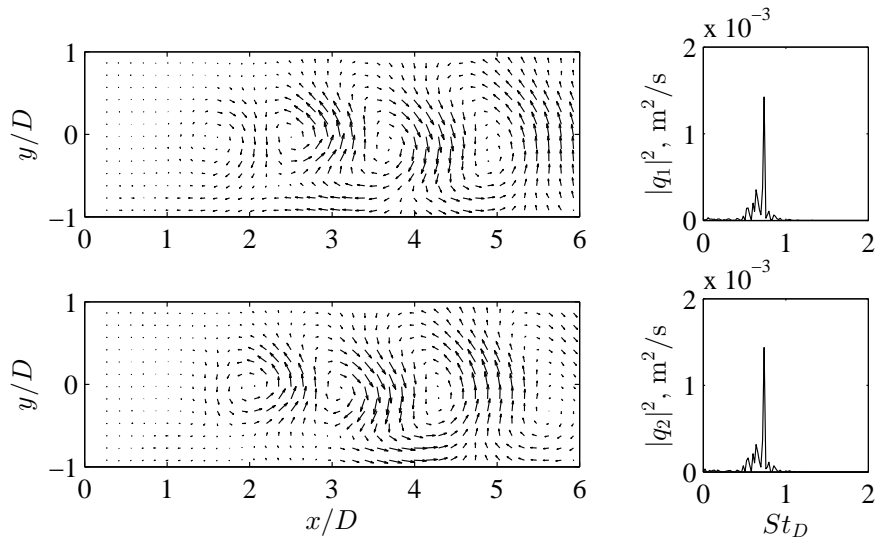


FIGURE 6. Most energetic pair of POD modes consisting of modes #1 and #2, for  $\rho_u/\rho_b = 1.7$  and  $U_{tip} = 30$  m/s. Spatial modes are illustrated on the left with velocity vector fields. Power spectral densities of the corresponding time-dependent POD coefficients for modes #1 and #2,  $|q_1|^2$  and  $|q_2|^2$ , are shown on the right.

## 5. Computational Results and Comparison

In this section, the predictions from the local stability analysis, applied around the mean flow, are compared with the flow dynamics measured experimentally. The validity of applying linear stability analysis to turbulent mean flows is still an area of active research. On the one hand, Reynolds & Hussain (1972) provided a theoretical basis by dividing the flow into a mean component, a periodic component, and a turbulent component. By considering a local stability analysis of a turbulent shear layer, they concluded that a turbulence model needs to be included in the stability analysis. On the other hand, other studies have obtained accurate results without using turbulence models. For example, Meliga *et al.* (2012) performed a linear stability analysis on the mean flow around a D-shaped cylinder at  $Re = 13000$ , using a frozen eddy viscosity approach. Their predicted frequency was reasonably close to that of their oscillating flow ( $\omega = 1.57$ , giving  $St = 0.25$ ). Mettot *et al.* (2014) performed a similar study on the same D-shaped cylinder but with molecular viscosity instead of a frozen eddy viscosity. Their predicted frequency was close to that of Meliga *et al.* (2012) and their predicted growth rate was also positive ( $\sigma = 0.26$ ). Given the success of Mettot *et al.* (2014) at predicting frequency and spatial structure without turbulence models in a configuration close to ours, we also use only molecular viscosity in our stability analysis. It is interesting to note that Barkley (2006) also performed a stability analysis around the mean flow behind a cylinder at  $Re = 45$  to 180. Like Meliga *et al.* (2012), Barkley found that this produces an eigenmode with the same frequency as the original oscillating flow, but with zero growth rate. In this case, however, turbulent models would not be appropriate because the flow, although oscillating, was laminar.

The main focus of the studies by Meliga *et al.* (2012) and Mettot *et al.* (2014), was to perform sensitivity analysis of the flow by combining the direct and adjoint eigenfunctions of the most unstable eigenmodes. They were not as concerned with the growth rate. In this section, we start by computing the linear global mode frequency, growth rate, and mode shapes around the time-averaged experimental data and then comparing the results with the full experimental data. This reveals whether the stability analysis can predict the correct frequency and mode shape, which is a pre-requisite for finding the eigenvalue sensitivity, discussed in Section 5.2. During this process, we also examine the growth rate because we find the same relationship between (i) the linear global mode growth rate and (ii) the nonlinear limit cycle amplitude that is expected for laminar flows near a Hopf bifurcation.

### 5.1. Local Stability Analysis

Figure 7 (top) compares the streamwise dependence of the absolute frequency,  $\omega_{0,r}/2\pi$ , (dashed lines) with the measured global mode frequency (solid lines). Figure 7 (bottom) plots the absolute growthrate,  $\omega_{0,i}$  and reveals a pocket of absolute instability around  $0.2 < x/D < 2$ . The stability analysis correctly captures that higher bluff body lip velocities lead to higher frequencies.

The linear global mode frequency and growth rate,  $f_{g,l}$  and  $\omega_g$ , are calculated by finding the saddle point of  $\omega_0$  in the complex  $X$ -plane, as described in section 2. Figure 8a compares the predicted global mode frequency,  $f_{g,l}$ , with the experimentally-measured frequency,  $f_{g,m}$ . These are compared for various values of the lip velocity at six different density ratios. This comparison shows that the local linear analysis consistently under-predicts the frequency by around 15%, across all density and velocity ratios. This can be compared with the global linear analysis of Barkley (2006), which slightly under-predicts the frequency and the global linear analyses of Meliga *et al.* (2012); Mettot *et al.* (2014), which over-predict the frequency by around 10%. Regarding local analyses, the same 10

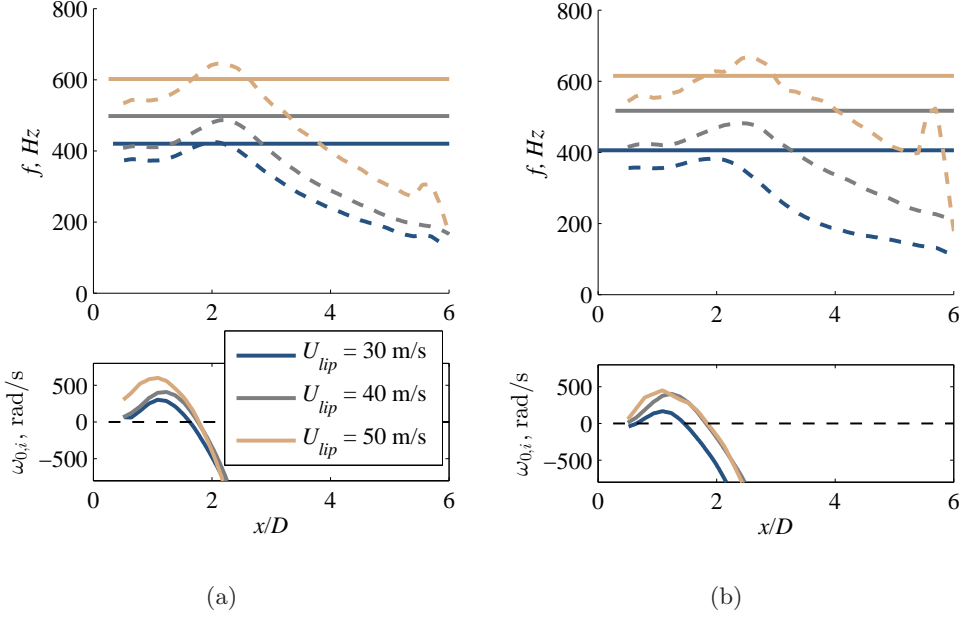


FIGURE 7. Top: Comparison of the measured global mode frequency (solid lines) and the predicted absolute frequency (dashed lines). Bottom: For reference, the absolute growthrate is shown. The left column is for a fixed density ratio of  $\rho_u/\rho_b = 1.7$  and the right column is for a fixed density ratio of  $\rho_u/\rho_b = 2.0$

to 15% under-prediction of the frequency was seen in a local analysis by Juniper *et al.* (2011) for a uniform density wake flow in a channel at  $Re = 100$ . Similarly, a smaller under-prediction was seen by Giannetti & Luchini (2007) for the local analysis of the flow around a cylinder, but only for Reynolds numbers greater than 80. Interestingly, the degree of accuracy in the frequency is similar to that of previous studies based on analyses around the mean flow, but for studies that determined the base flow with RANS simulations rather than experiments.

Another way to estimate the global mode frequency from the local analysis is to use the frequency selection criterion from the nonlinear wave front theory of Pier & Huerre (1996). The nonlinear wave front theory predicts that the experimentally measured frequency and spatial growth rate should match those predicted by the local analysis at the streamwise position where the flow transitions from convective to absolute instability. Therefore, the global mode frequency can be estimated from the absolute frequency,  $\omega_{0,r}$ , at the upstream point of  $\omega_{0,i} = 0$ . Figure 8b compares the frequency predicted from the nonlinear wavefront theory,  $f_{g,nw}$ , to the experimentally measured frequency. The figure shows a slight underprediction of the global mode frequency similar to that observed from the saddle point approach.

Next we define the local energy of the oscillations,  $E(x)$ , by integrating the spectral energy of the measured streamwise and cross-stream velocity components from  $St_D = 0.20$  to  $St_D = 0.28$ , and then integrating this across the transverse dimension,  $y$ , from the flow centerline to the channel wall:

$$E(x) = \int_y \int_{0.20}^{0.28} (|u(x, y, St_D)|^2 + |v(x, y, St_D)|^2) dSt_D dy \quad (5.1)$$

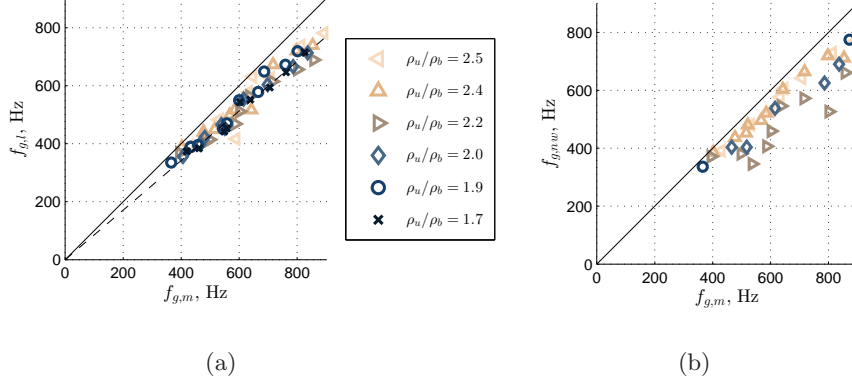


FIGURE 8. Comparison of measured and predicted global mode frequencies, from velocity sweeps at six different density ratios. Part (a) compares measured global mode frequencies,  $f_{g,m}$  to those predicted from saddle point of  $\omega_0(X)$  approach,  $f_{g,l}$ . Solid line corresponds to  $f_{g,l} = f_{g,m}$ . Dashed line is least squares fit to the slope of  $f_{g,l}$  vs  $f_{g,m}$ . Part (b) compares measured global mode frequencies to those predicted from nonlinear wave front theory,  $f_{g,nw}$ . Cases where the PIV measurement was noisy near the transition point from convective to absolute instability were omitted from part (b).

Figure 9 compares  $E(x)$  (top) with the local absolute growth rate  $\omega_{0,i}$  (bottom) at two values of  $U_{lip}$ . The energy of the oscillations grows rapidly in the absolutely unstable region. Therefore, we hypothesize that the oscillations at the global mode frequency are generated by hydrodynamic feedback mechanisms in the absolutely unstable region. Furthermore, the oscillations' energy increases as the linear global mode growth rate increases. This relationship can be examined more precisely by assuming that the complex amplitude,  $A$ , of the oscillations can be modelled by the Stuart-Landau equation (Landau 1944; Stuart 1958; Provansal *et al.* 1987):  $dA/dt = \omega_{g,i}A - \beta|A|^2A$ . This is a good approximation when the operating point is close to that of the onset of oscillations, which is not always the case here. Saturation is achieved when  $dA/dt = 0$ , which leads to the relation that  $|A|^2 \propto \omega_{g,i}$ , where  $A^2 \propto E$ , as defined above. Figure 10 plots the maximum of  $E$  against  $\omega_{g,i}$  (calculated from the local linear analysis) for five values of  $U_{lip}$  and three values of  $\rho_u/\rho_b$ . The fact that  $E$  is proportional to  $\omega_{g,i}$  shows that the linear growth rate, which is calculated here around the turbulent mean flow, has the same relationship to the nonlinear saturated amplitude as that which would be expected for a laminar base flow. This is a surprising result, especially given that the growth rates calculated from global analyses by Barkley (2006); Meliga *et al.* (2012); Mettot *et al.* (2014) do not have this characteristic.

Figures 9 and 10 also show that the stability analysis correctly captures the role of the density ratio: lower density ratios lead to higher absolute growth rates and larger limit cycle amplitudes in this flow. The density ratio at which the flow becomes unstable,  $\rho_u/\rho_b|_{crit}$ , can be calculated from this data by extending the Stuart-Landau model described above. If the linear growth rate,  $\omega_{g,i}$ , is proportional to  $\rho_u/\rho_b - \rho_u/\rho_b|_{crit}$ , and  $|A|^2 \propto \omega_{g,i}$ , then  $|A|^2 \propto \rho_u/\rho_b - \rho_u/\rho_b|_{crit}$ . Figure 11 plots  $\max(E)$  against  $\rho_u/\rho_b$ , showing a satisfactorily linear relationship for each lip velocity  $U_{lip}$ . Least squares lines are overlaid for each velocity in order to extrapolate to  $E = 0$ . This shows that the critical

density ratio is in the range  $\rho_u/\rho_b = 2.6 - 2.8$ , and is relatively insensitive to  $U_{lip}$ , as is expected.

Figure 9 also shows that the amplitude of the oscillations increases in the absolutely unstable region and that the maximum spatial growth rate coincides approximately with the point of maximum absolute instability. This can be examined more precisely by comparing the spatial growthrate from the local analysis with that from the experimental measurements. In order to obtain the spatial growthrate from experiments, we assume a linear, normal modes form for the streamwise and transverse global mode velocity components,  $(u, v) = (|\hat{u}|, |\hat{v}|)\exp[-i(\omega t - kx)]$ . Next, we recall that the global mode energy has the general form,  $E = \int_0^H (|u|^2 + |v|^2) dy$ . Finally, we differentiate to obtain the spatial growthrate,  $-2k_i = d \ln(E)/dx$ . Figure 12 compares the streamwise dependence of the spatial growthrate derived from the local analysis (solid line) and from the experiments (dashed line). The spatial growth rates from the local analysis are composed of the  $k^+$  and  $k^-$  branches, computed for the predicted global mode frequency,  $f_{g,l}$ . The  $k^-$  branch is selected in the region upstream of the wavemaker, and the  $k^+$  branch is selected downstream of the wavemaker. In a local analysis around a steady flow, the two should match well in the low amplitude region upstream, where the growth is linear, but would not be expected to match in the high amplitude region downstream. In the local analysis around the time-averaged flow shown here, however, the two match reasonably well upstream (particularly for the  $U_{lip} = 60$  cases) but match even better in the high amplitude region downstream. This shows that, given a mean flow, the linear local analysis can predict the local spatial growth rate and therefore is likely to give a correct mode shape. Although this is something of a circular argument, because the mean flow was generated from the mode shape in the first place, it is reassuring for the next stage in this analysis, which is to calculate the direct and adjoint global modes from the local linear analysis.

Recalling the nonlinear wave front theory of Pier & Huerre (1996), the measured and predicted linear spatial growth rates are expected to match at the point where the flow transitions from convective to absolute instability. Figure 12 identifies this point with a  $\star$  symbol. The figure shows a good match between experiment and prediction at this point for the 60 m/s cases, and a poorer match for the 30 m/s cases. The reason for the poor comparison (as well as for the scatter in the nonlinear wave front frequencies in 8b) is unknown, but the authors suspect that it is due to the higher measurement uncertainty of the fluctuating velocity at this spatial position (as quantified by the error bars).



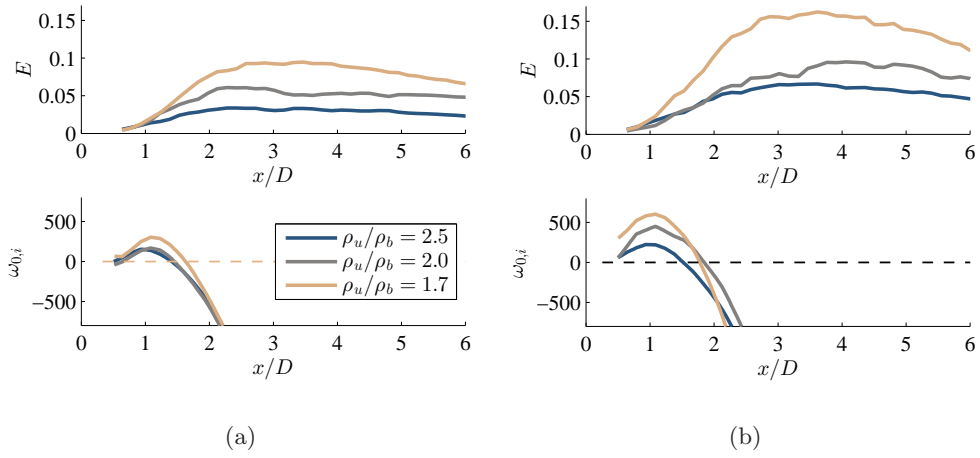


FIGURE 9. Axial dependence of the oscillatory kinetic energy,  $E$  (Top), and Predicted absolute growthrate (Bottom). Results are shown for density ratio sweeps at fixed velocities of  $U_{iip} = 30$  m/s (left column) and  $U_{iip} = 50$  m/s (right column). As expected, the amplitude of the mode grows most rapidly in the region of strong absolute instability.

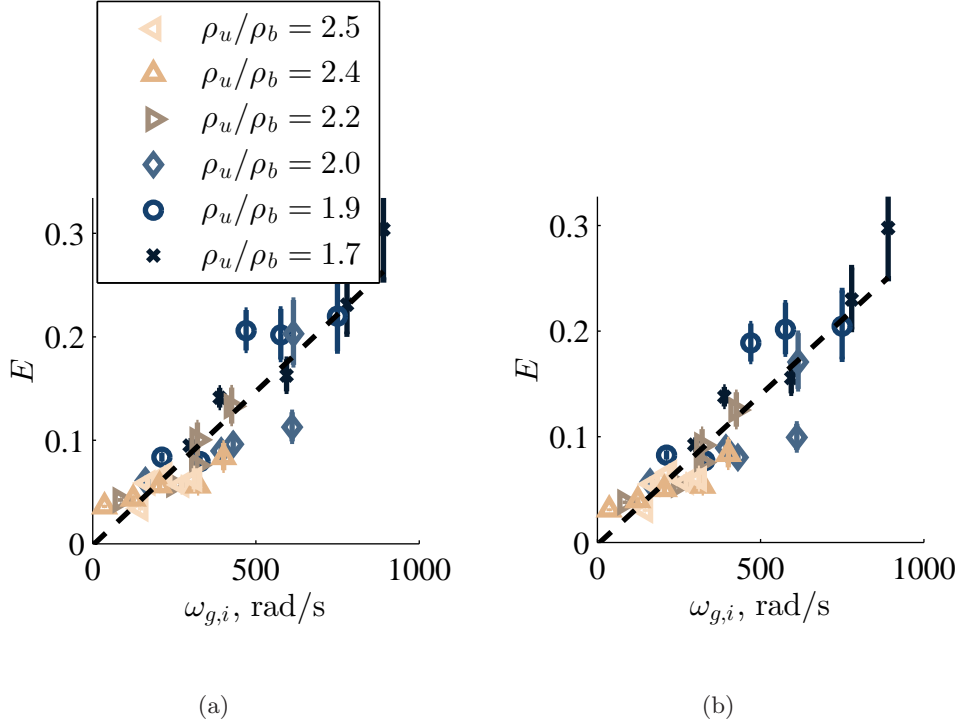


FIGURE 10. Maximum of the oscillatory kinetic energy,  $E(x)$  plotted as a function of the linear global mode growthrate. This is shown for a combination of five values of  $U_{lip}$  and six values of  $\rho_u/\rho_b$  and for  $\max(E)$  (left) and for  $E(x/D = 3.0)$  (right). The dashed line is a linear least-squares fit. The error bars represent PIV measurement uncertainty due to the Stokes number considerations discussed in Section 3.2.

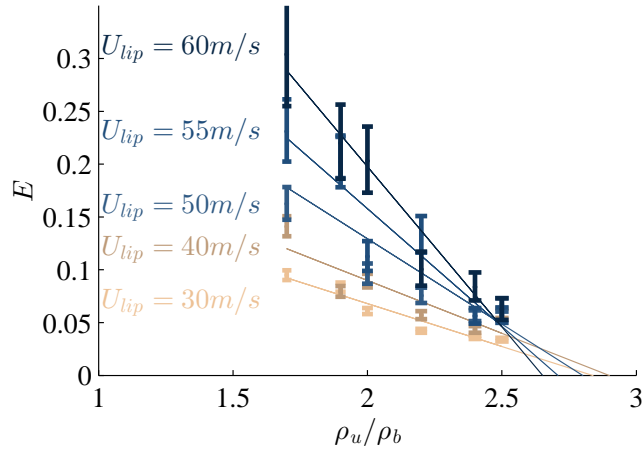


FIGURE 11. Maximum of the oscillatory kinetic energy,  $E(x)$ , plotted as a function of the density ratio, shown for a combination of five values of  $U_{lip}$  and six values of  $\rho_u/\rho_b$ . Linear least-squares fit lines are overlaid for each velocity. The error bars represent PIV measurement uncertainty due to the Stokes number considerations discussed in Section 3.2.

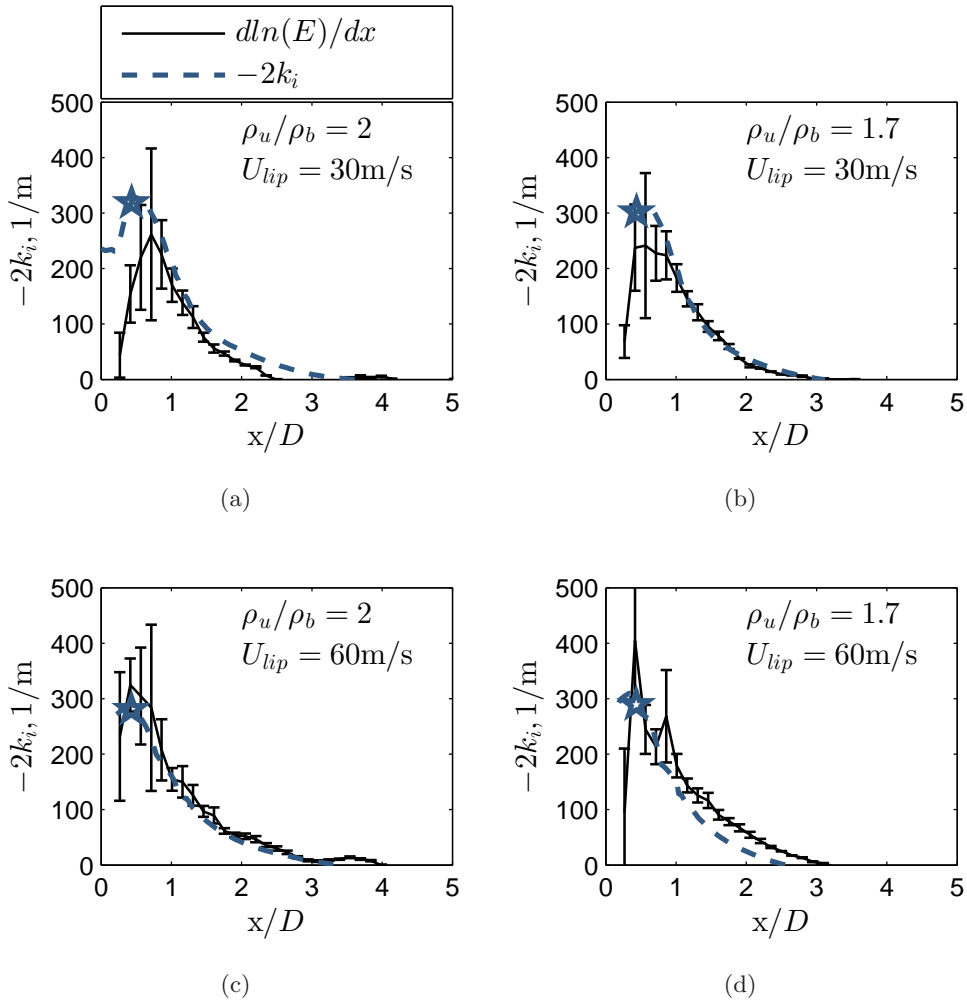


FIGURE 12. Comparison of predicted linear spatial growthrate to measured spatial growthrate. Symbol  $\star$  is placed at the streamwise position where linear stability analysis predicts the transition from convective to absolute instability (the upstream boundary of the pocket of absolute instability). The error bars represent PIV measurement uncertainty due to the Stokes number considerations discussed in Section 3.2.

This section showed comparisons between stability analysis predictions using an experimentally measured base flow, and the experimentally measured flow oscillations. The comparisons show good qualitative trends in the predictions, with small quantitative discrepancies. Three sources of error may account for these discrepancies. These potential sources of error, discussed in detail in Sections 2 and 3.2, are uncertainty in the measured base flow (which propagates through the stability analysis), errors inherent to the stability analysis procedure, and uncertainty in the measured oscillatory velocity. Experimental uncertainty in the oscillatory frequency is extremely small, and uncertainty in the oscillatory velocity amplitude is quantified and indicated with error bars. The authors hypothesize that discrepancies beyond these error bars are due to errors that are inherent to the stability analysis, not due to the small uncertainty in the measured base flow. The weakest components of the analysis procedure are the parallel flow assumption, and the use of a time averaged turbulent flow field as the base flow. The influence of the parallel flow assumption could be investigated in future work with a full global analysis.

### 5.2. Direct global mode, adjoint global mode, and wavemaker

The aim of this section is to compare the predicted (linear) 2D global mode shape to the measured (nonlinear) 2D global mode shape, and to obtain the adjoint global mode and the eigenvalue sensitivity,  $\lambda$ . This analysis, which is performed around the time-averaged mean flow is similar to that of Meliga *et al.* (2012), which included a frozen eddy viscosity, and Mettot *et al.* (2014), which used only molecular viscosity. These analyses were compared with the experimentally-derived sensitivities by Parezanovic & Cadot (2012) and found to give excellent predictions of the oscillation's sensitivity to the addition of a passive control element.

The measured global mode shape is obtained by conditionally averaging the velocity field at a fixed phase of the global mode oscillation. To accomplish this, the mean-subtracted transverse velocity time series from a single spatial point is locally fitted to a sinusoid with a fixed frequency of  $f_n = 0.24U_{lip}/D$  over two period windows (Emerson *et al.* 2012). The phases of these sinusoidal fits are stored as a time-dependent signal. This signal is then used as a reference phase, to conditionally average the entire velocity field at instants that correspond to a fixed reference phase.

An example snap-shot (ie, a single phase) of the conditionally averaged transverse velocity is shown in the top frame of Figure 13 for the upper half of the channel. The direct global mode shape is presented in the frame immediately below. Comparison between these two shows qualitatively similar transverse mode shapes. For a more quantitative comparison of the global mode to the experimental measurement, Figure 14 compares the axial dependencies of the phases of the linear global mode and conditionally averaged transverse velocity. The experimentally measured phase was determined by first performing a Fast Fourier Transform (fft) of the transverse velocity at every spatial position. Next, the phase was extracted from the transverse velocity Fourier coefficients,  $\hat{v}$ , at the global mode frequency,  $f_{g,m}$ , and at a transverse position of  $y/D = 0$ . As such, for the experimental measurement, we define the phase as  $\theta(x) = \angle \hat{v}(x, y/D = 0, f = f_{g,m})$ . For both the stability analysis and the experimental measurement, the bottom frame of Figure 14 shows the phase speed, which is representative of the convective velocity, and which is calculated from finite differencing the axial dependence of the phase. The phase speed is calculated as

$$U_c(x) = 2\pi f_g \frac{\Delta x}{\Delta \theta} \quad (5.2)$$

where  $\Delta x$  represents a finite difference of axial position, and  $\Delta \theta$  represents a finite difference of the phase. The figure shows that the linear stability analysis captures the

qualitative trend of an accelerating phase speed with increasing axial position. Additionally, the figure shows close quantitative agreement, although the stability analysis appears to slightly over-predict the phase speed. This overprediction of the phase speed is also evident in Figure 13, which suggests a slightly longer axial wave length for the prediction, relative to the experiment. As a quantitative comparison of the magnitudes of the predicted and measured global modes, the reader is referred to the spatial growth rates plotted in Figure 12, which shows the same case as Figures 13 and 14.

The adjoint global modes for streamwise and transverse velocity perturbations are shown in the third and fourth frames of 13. These quantify the influence that open loop velocity forcing has on the oscillation amplitude, as shown by the final term in equation (9) of Chomaz (2005). For example, this shows that the global mode is most sensitive to open loop velocity forcing in the shear layers aft of the bluff body and that it is slightly more sensitive to streamwise forcing than transverse forcing. Finally, the eigenvalue sensitivity,  $\lambda$  is shown in the last frame. The values of  $\lambda$  shown here are the products of the direct and adjoint global mode velocity magnitudes,  $\lambda = \sqrt{|u|^2 + |v|^2} \times \sqrt{|u^\dagger|^2 + |v^\dagger|^2}$ . This quantity physically represents the eigenvalue drift caused by a device that produces an extra acceleration (ie, momentum feedback) at a given point in space. This is large in locations that have both significant oscillation amplitude (contained in the direct global mode), and significant sensitivity to oscillations (contained in the adjoint global mode), and therefore identifies the location where a passive feedback device would have most influence if it affects the perturbation but not the base flow. This is the wavemaker region of the flow. Notice that for this flow, the wavemaker is located in the recirculation zone of the wake, between  $x/D = 1$  and  $x/D = 2$ .

This study pursues the eigenvalue sensitivity to momentum feedback, defined above as  $\lambda$ . However, it is important to note that there are many different ways to define the eigenvalue sensitivity, each of which describes the eigenvalue drift caused by a different type of feedback. As a practical example, the quantity  $\lambda/\rho_0$  would physically represent the eigenvalue drift due to a device that causes an extra force-feedback at a point in space. Although not shown here for reasons of space, analysis of this scenario reveals a nearly identical wavemaker region, due to the fact that the wavemaker region lies almost entirely in the uniform-density combustion products region.

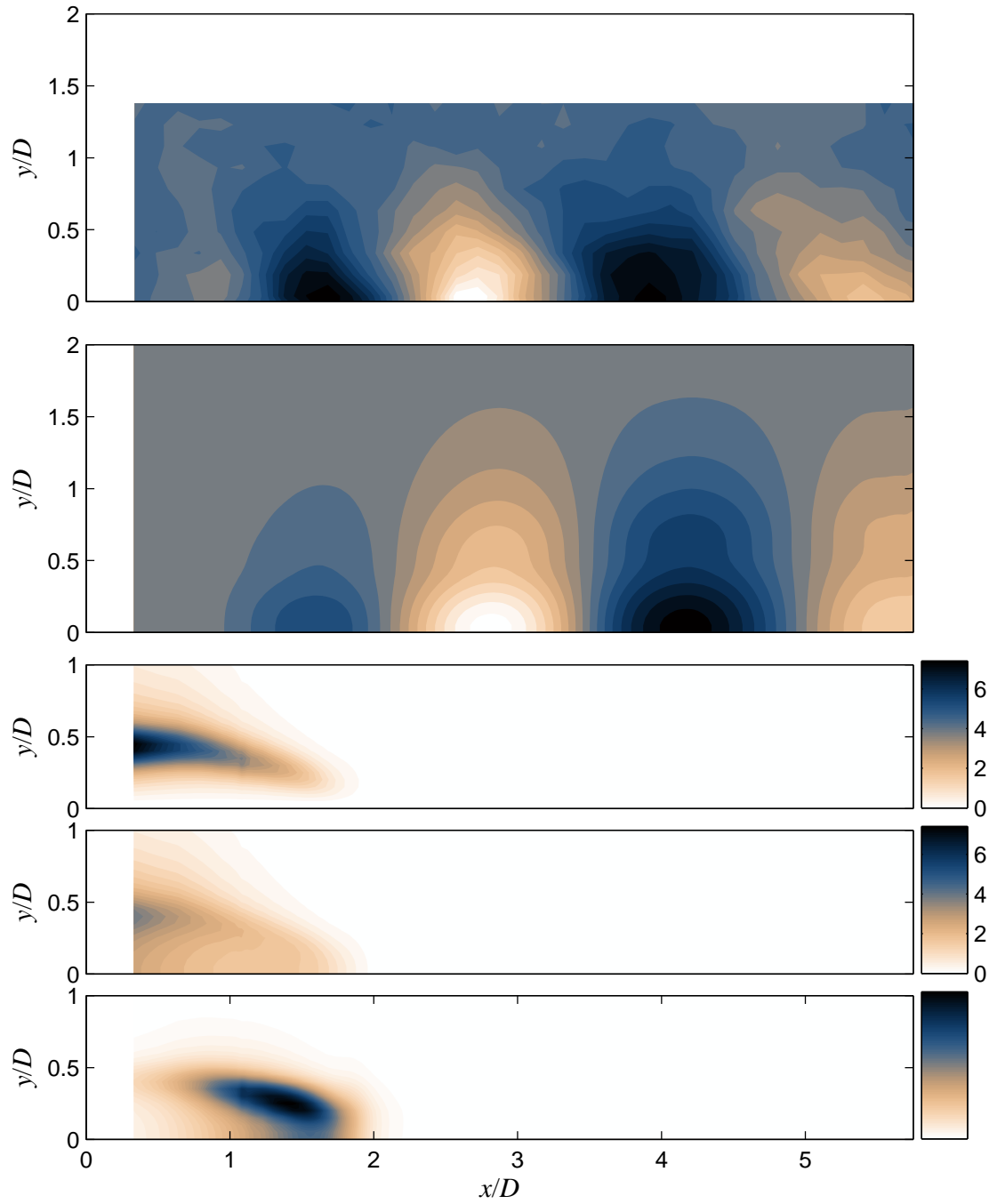


FIGURE 13. Sinuous mode shape, showing from top to bottom: instantaneous measured global mode showing conditionally averaged transverse velocity, instantaneous linear direct global mode shape showing transverse velocity,  $v$ , adjoint global mode showing receptivity to streamwise velocity forcing,  $|u^\dagger|$ , adjoint global mode showing receptivity to transverse velocity forcing,  $|w^\dagger|$ , eigenvalue sensitivity,  $\lambda$ . Conditions are  $\rho_u/\rho_b = 1.7$ ,  $U_{tip} = 30$  m/s

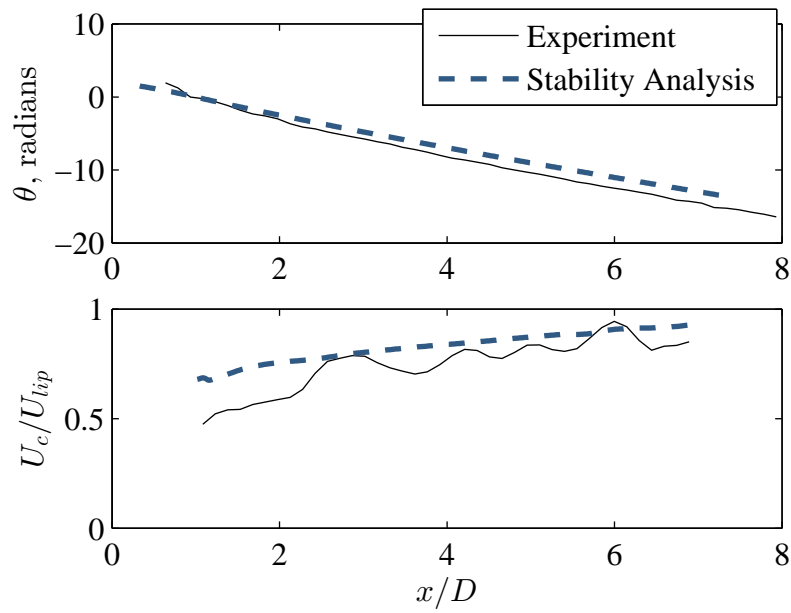


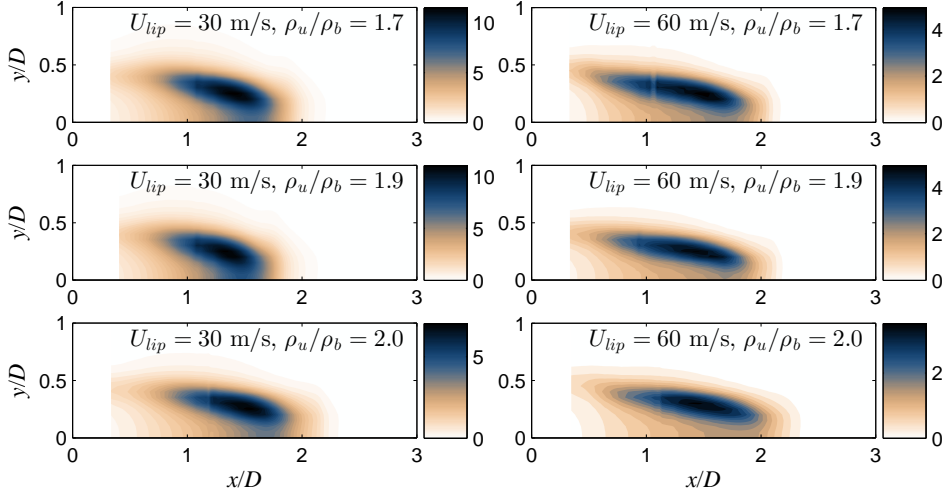
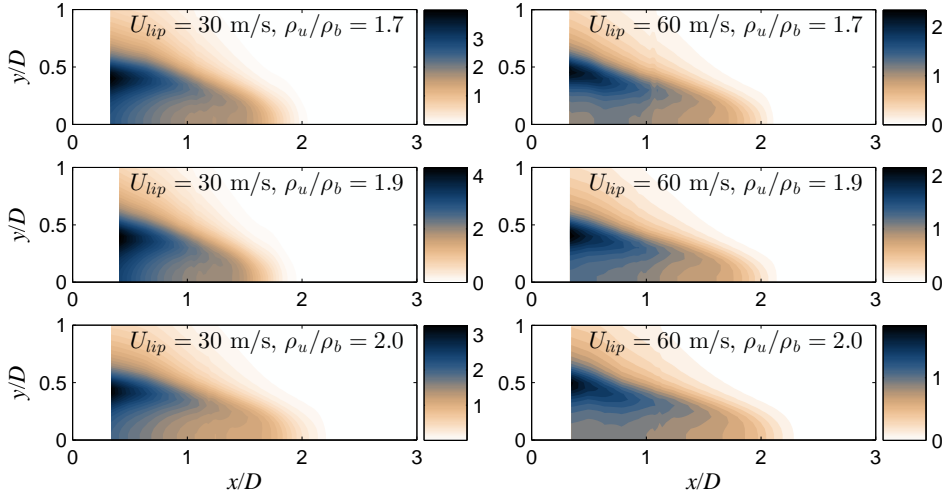
FIGURE 14. Phase speed (top) and phase velocity (bottom) of the experimentally measured and the predicted mode shapes of the fluctuating transverse velocity. Conditions are  $\rho_u/\rho_b = 1.7$ ,  $U_{tip} = 30$  m/s

### 5.3. Influence of density ratio and lip velocity on wavemaker region and receptivity regions.

Figure 15 presents a comparison of the wavemaker region for three density ratios and two lip velocities. The left column is a density ratio sweep at a fixed lip velocity of  $U_{lip} = 30$  m/s, and the right column is a density ratio sweep at a fixed lip velocity of  $U_{lip} = 60$  m/s. The figure shows that the wavemaker shape and location is relatively insensitive to these two parameters, even though the growth rates, frequencies, and amplitudes vary significantly, as shown earlier. The most noticeable influence is the slight elongation of the wavemaker region with increases in bluff body lip velocity. There also appears to be slight elongation of the wavemaker region with increase in density ratio, which is apparent when comparing the  $\rho_u/\rho_b = 1.7$  cases to the  $\rho_u/\rho_b = 2.0$  cases. These effects are probably due to the slight increase in recirculation zone length with increases in lip velocity and density ratio (Emerson *et al.* 2012), and support the observation from the end of section 5.2, as well as that from analyses around steady flows (Giannetti & Luchini 2007) that the wavemaker is centred on the recirculation zone.

Figure 16 presents a comparison of the receptivity to transverse velocity forcing (the adjoint mode). This region follows the edge of the time-averaged recirculation region, which varies slightly as the lip velocity and density ratio change.




 FIGURE 15. Comparison of the sinuous mode eigenvalue sensitivity,  $\lambda$ , for several velocities and density ratios

 FIGURE 16. Comparison of the sinuous mode receptivity to transverse velocity forcing,  $|v^\dagger|$ , for several velocities and density ratios

#### 5.4. Varicose oscillations

The previous sections concerned the sinuous mode, which is the observed wake mode in the absence of external forcing or thermoacoustic oscillations. However, varicose oscillations may be excited by external forcing. For example, experimental work by Emerson *et al.* (2013) demonstrated that varicose oscillations often dominate in longitudinal combustion instabilities of bluff body combustors. Therefore, the stability of the varicose mode has direct application to the combustion instability problem. While the stability analysis does not model the acoustically coupled, global thermo-acoustic system, it does reveal the most significant sensitivities of the hydrodynamic component of such a system,

from which one may speculate about the overall system. For example, Figure 17 will show that the hydrodynamic response to acoustic driving is much more sensitive to streamwise forcing than to transverse forcing, and that the highest eigenvalue sensitivity sits on the flow centreline just downstream of the bluff body. For this reason, this section explores the stability of varicose oscillations around the time-averaged flow calculated from the experimental data.

It is worth noting that the predominant unsteady feature in the experimental data is a sinuous mode. Therefore this analysis is pertinent to varicose oscillations occurring on top of a flow that is already oscillating sinuously. An important point when considering a linear interpretation of such a situation is for the two modes to oscillate independently at different time scales. For the conditions presented in this section ( $\rho_u/\rho_b = 1.7$ ,  $U_{lip} = 30\text{m/s}$ ), the predicted frequency of the varicose global mode is 35 Hz, which is an order of magnitude lower than the 374 Hz frequency predicted for the sinuous global mode.

Figure 17 shows (a–b) the direct global mode, (c–d) the receptivities to streamwise and transverse velocity forcing, and (e) the wavemaker of the varicose mode. The varicose mode shown in Figure 17 was computed for the same base flow as the sinuous mode shown previously in Figure 13. Comparing these two figures reveals some significant differences between the sinuous and varicose modes.

Firstly, the streamwise wavelength of the varicose direct global mode is much longer than that of the sinuous mode. Evidence of this has been observed previously in the direct numerical simulations of Biancofiore *et al.* (2014). Secondly, by comparing the relative amplitudes of the (c) streamwise and (d) transverse receptivities in figures 16 and 17, it can be seen that the varicose mode is much less sensitive to transverse forcing than the sinuous mode. Thirdly, although the varicose mode is similar to the sinuous mode in that it is very receptive to forcing in the shear layers, it is also receptive to streamwise velocity forcing along the centreline around  $x/D = 1$ . This implies that the growth rate of the varicose oscillations could be reduced (or the damping rate increased) by streamwise injection from the body at  $y/D = 0$ , while minimally affecting the sinuous oscillation. In a system that is forced in a varicose manner, e.g. by thermoacoustic oscillations, this would reduce the amplitude of the hydrodynamic oscillations and thereby weaken the feedback mechanism between the acoustics and heat release. Fourthly, the wavemaker region of the varicose mode has highest amplitude at  $y/D = 0$ , while that of the sinuous mode is at  $y/D = 0.25$ . Additionally, there is a separate, distinct, weaker wavemaker region in the shear layer. This tendency of the varicose mode to have two distinct receptivity regions and wavemaker regions was not present in the sinuous mode, and is consistent when varying  $\rho_u/\rho_b$  and  $U_{lip}$ .

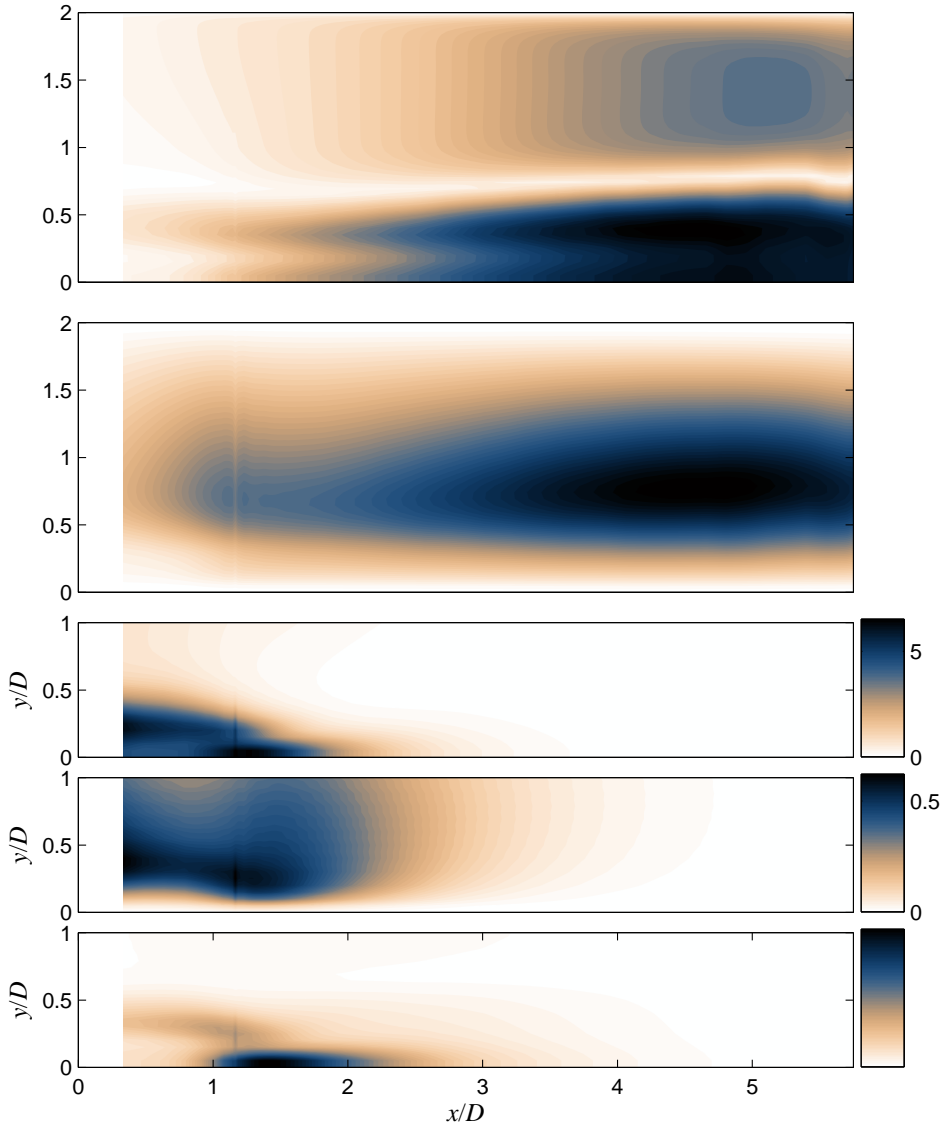


FIGURE 17. Varicose mode shape, showing from top to bottom: direct streamwise velocity global mode,  $u_r$ , direct transverse velocity global mode,  $v$ , adjoint global mode showing receptivity to streamwise velocity forcing,  $|u^\dagger|$ , adjoint global mode showing receptivity to transverse velocity forcing,  $|v^\dagger|$ , eigenvalue sensitivity,  $\lambda$ . Conditions are  $\rho_u/\rho_b=1.7$ ,  $U_{lip} = 30$  m/s. Colorbar for  $|v^\dagger|$  is  $1/10^{\text{th}}$  the colorbar of  $|u^\dagger|$  for visibility purposes.

## 6. Conclusions

This study examines the receptivity and sensitivity of the oscillating flow behind a flame holder in the presence of combustion. A local stability analysis is used in order to calculate the direct and adjoint linear global modes about the experimentally-derived time-averaged base flow. This procedure has been applied to laminar nonreacting wakes (Juniper & Pier 2015) and has been shown to give a very good approximation to the modes found from a global analysis, particularly for nearly-parallel flows such as this.

The direct global modes calculated from the local stability analysis have similar frequencies, mode shapes, phase speeds, and streamwise growth rates as the experimentally-observed oscillations over a wide range of flame density ratios and bluff body lip velocities. This provides a sound basis on which to form the adjoint global modes for the receptivity and sensitivity analysis. In addition, the linear local analysis predicts a global growth rate that is proportional to the square of the experimentally-measured amplitude of oscillation, in accordance with a Stuart-Landau model. This feature was not found in the linear global analyses of Barkley (2006); Meliga *et al.* (2012); Mettot *et al.* (2014), which were also around the time-averaged mean flow.

The adjoint global modes show where the flows are most receptive to external forcing. For sinuous oscillations, the flow is slightly more receptive to streamwise forcing than to transverse forcing and is most receptive in the shear layers just downstream of the bluff body edges. For varicose oscillations, the flow is much more receptive to streamwise forcing than to transverse forcing. It is quite receptive in the shear layers, but it is most receptive along the centreline, although only to streamwise forcing. The overlap of the direct and adjoint global modes show where the flows are most sensitive to changes in internal feedback, which is the wavemaker region. For both sinuous and varicose oscillations, this region is at around  $x/D = 1.5$ .

The regions of high receptivity and sensitivity change very little as the density ratio and lip velocity change. However, the stability analysis shows that increasing the density ratio reduces the global mode growthrate and has little influence on the global mode frequency. This stabilizing influence is reflected in the experiments, in which the limit cycle amplitude reduces when the density ratio increases. The stability analysis also shows that increasing the bluff body lip velocity causes a proportional increase in the global mode frequency, which compares well with the experimentally measured global mode frequency.

This study performs a local stability analysis on experimentally-derived time-averaged velocity profiles in a slowly-developing wake flow. The authors implement the techniques described in Juniper & Pier (2015) to extract the direct and adjoint global modes from the local analysis. These modes show the regions of the flow that are most receptive to external forcing and sensitive to changes in internal feedback. For the combustor flow behind a bluff body studied here, this analysis shows that the sinuous mode is more hydrodynamically unstable than the varicose mode and that the varicose mode has a much lower frequency and longer wavelength. Nevertheless, the varicose mode can lock into longitudinal oscillations in practical combustion systems and thereby cause thermoacoustic oscillations. The varicose mode is quite receptive to momentum forcing in the shear layers downstream of the bluff body. A longitudinal acoustic mode would have high amplitude in these regions, which reveals how this type of acoustics couples to the flame effectively. The varicose mode is most receptive to streamwise momentum forcing along the centreline, however, where the sinuous mode is insensitive to forcing. This provides physical insight into the reasons behind the behaviour of this flow, and suggests a control strategy involving streamwise forcing behind the bluff body, either with feedback control or with a passive device. Such a strategy might change the varicose mode, which is dangerous for thermoacoustics, without affecting the sinuous mode, which is good for mixing.

Matthew Juniper acknowledges the financial support of the European Research Council under grant 2590620. Tim Liewwen acknowledges the support of the University Turbine Systems Research (contract #DE-FC21-92MC29061) program under contract monitor Dr. Mark Freeman, and the Air Force Office of Scientific Research (contract #FA9550-12-1-0107/RC657), under contract monitor Dr. Chiping Lee.

REFERENCES

- BARKLEY, D. 2006 Linear analysis of the cylinder wake mean flow. *Europhysics Letters* **75**, 750–756.
- BERKOOZ, GAL, HOLMES, PHILIP & LUMLEY, JOHN 1993 The proper orthogonal decomposition in the analysis of turbulent flows. *Annual Review of Fluid Mechanics* **25**, 539–575.
- BIANCOFIORE, LUCA, GALLAIRE, F., LAURE, P. & HACHEM, ELIE 2014 Direct numerical simulations of two-phase immiscible wakes. *Fluid Dynamics Research* **46**, 041409.
- CARDELL, GREGORY SCOTT 1993 Flow past a circular cylinder with a permeable wake splitter plate. PhD thesis, California Institute of Technology.
- CHOMAZ, JEAN-MARC 2005 Global instabilities in spatially developing flows: Non-normality and nonlinearity. *Annual Review of Fluid Mechanics* **37**, 357–392.
- CROSS, CALEB, FRICKER, AIMEE, SHCHERBIK, DMITRIY, LUBARSKY, EUGENE, ZINN, BEN T. & LOVETT, JEFFERY A. 2010 Dynamics of non-premixed bluff body-stabilized flames in heated air flow. In *ASME Turbo Expo*.
- EMERSON, BENJAMIN 2013 Dynamical characteristics of reacting bluff body wakes. PhD thesis, Georgia Institute of Technology, School of Aerospace Engineering.
- EMERSON, BENJAMIN, MURPHY, KELVIN & LIEUWEN, TIM 2013 Flame density ratio effects on vortex dynamics of harmonically excited bluff body stabilized flames. In *ASME Turbo Expo*.
- EMERSON, BENJAMIN, O’CONNOR, JACQUELINE, JUNIPER, MATTHEW & LIEUWEN, TIM 2012 Density ratio effects on reacting bluff-body flow field characteristics. *J. Fluid Mech.* **706**, 219–250.
- ERICKSON, R. R., SOTERIOU, M. C. & MEHTA, P. G. 2006 The influence of temperature ratio on the dynamics of bluff body stabilized flames. In *44th AIAA Aerospace Sciences Meeting & Exhibit*.
- FINCHAM, A. M. & SPEDDING, G. R. 1997 Low cost, high resolution dpiv for measurement of turbulent fluid flow. *Experiments in Fluids* **23**, 449–462.
- FRANSSON, JENS HM, KONIECZNY, P & ALFREDSSON, PER HENRIK 2004 Flow around a porous cylinder subject to continuous suction or blowing. *Journal of Fluids and Structures* **19** (8), 1031–1048.
- GARNAUD, X., LESSHAFFT, L., SCHMID, P. J. & HUERRE, P. 2013 Modal and transient dynamics of jet flows. *Physics of Fluids* **25**, 044103.
- GIANNETTI, FLAVIO & LUCHINI, PAOLO 2007 Structural sensitivity of the first instability of the cylinder wake. *J. Fluid Mech.* **581**, 167–197.
- GÜLDER, Ö., SMALLWOOD, GREGORY, WONG, ROGER, SNELLING, D. R., SMITH, ROGER, DESCHAMPS, B. M. & SAUTET, J-C. 2000 Flame front surface characteristics in turbulent premixed propane/air combustion. *Combustion and Flame* **120**, 407–416.
- HILL, D. C. 1992 A theoretical approach for analysing the restabilization of wakes. *Tech. Rep.* 103858. NASA Technical Memorandum.
- HUERRE, PATRICK & MONKEWITZ, PETER 1990 Local and global instabilities in spatially developing flows. *Ann. Rev. Fluid Mech.* **22**, 473–537.
- HUERRE, PATRICK & MONKEWITZ, PETER 2000 Open shear flow instabilities. In *Perspectives in fluid dynamics : a collective introduction to current research* (ed. G. K. Batchelor, H. K. Moffat & M. G. Worster). C. U. P.
- J. NOGUERIA, A. LECUONA, P. A. RODRIGUEZ 1997 Data validation, false vectors correction and derived magnitudes calculation on piv data. *Measurement Science and Technology* **8**, 1493–1501.
- JUNIPER, M. 2006 The effect of confinement on the stability of two-dimensional shear flows. *J. Fluid Mech.* **565**, 171–195.
- JUNIPER, M. & CANDEL, S. 2003 The stability of ducted compound flows and consequences for the geometry of coaxial injectors. *J. Fluid Mech.* **482**, 257–269.
- JUNIPER, MATTHEW & PIER, BENOIT 2015 The structural sensitivity of open shear flows calculated with a local stability analysis. *European Journal of Mechanics-B/Fluids* **49**, 426–437.
- JUNIPER, MATTHEW P. 2012 Absolute and convective instability in gas turbine fuel injectors. In *ASME Turbo Expo*.
- JUNIPER, M. P., TAMMISOLA, O. & LUNDELL, F. 2011 The local and global stability of confined planar wakes at intermediate reynolds number. *J. Fluid Mech.* **686**, 218–238.

- KIEL, B., GARWICK, K., LYNCH, A., GORD, J. R. & MEYER, T. 2006 Non-reacting and combustor flow investigation of bluff bodies in cross flow. In *42nd AIAA/ASME/SAE/ASEE Joint Propulsion Conference & Exhibit*.
- KONSTANTINIDIS, E., BALABANI, S. & YIANNESKIS, M. 2007 Bimodal vortex shedding in a perturbed cylinder wake. *Physics of Fluids* **19**, 011701.
- LANDAU, L. D. 1944 On the problem of turbulence. *C. R. Acad. Sci. URSS* **44**, 311–314.
- LESSHAFFT, LUTZ & HUERRE, PATRICK 2007 Linear impulse response in hot round jets. *Phys. Fluids* **19**, 024102–1–024102–11.
- LIEUWEN, TIM 2012 *Unsteady Combustor Physics*. Cambridge University Press.
- LUCHINI, P., GIANNETTI, F. & PRALITS, J. 2009 Structural sensitivity of the finite-amplitude vortex shedding behind a circular cylinder. In *IUTAM Symposium on Unsteady Separated Flows and their Control* (ed. Marianna Braza & Kerry Hourigan), *IUTAM Bookseries*, vol. 14, pp. 151–160. Springer.
- MA, X., KARAMANOS, G.-S. & KARNIADAKIS, G. E. 2000 Dynamics and low-dimensionality of a turbulent near wake. *J. Fluid Mech.* **410**, 29–65.
- MARQUET, OLIVIER, SIPP, DENIS & JACQUIN, LAURENT 2008 Sensitivity analysis and passive control of cylinder flow. *J. Fluid Mech.* **615**, 221–252.
- MEI, R. 1996 Velocity fidelity of flow tracer particles. *Experiments in Fluids* **22**, 1–13.
- MELIGA, OPHILIPPE, SIPP, DENIS & CHOMAZ, JEAN-MARC 2008 Absolute instability in axisymmetric wakes: compressible and density variation effects. *J. Fluid Mech.* **600**, 373–401.
- MELIGA, PHILIPPE, PUJALS, GREGORY & SERRE, ERIC 2012 Sensitivity of 2-d turbulent flow past a d-shaped cylinder using global stability. *Physics of Fluids* **24**, 061701.
- MELLING, A. 1997 Tracer particles and seeding for particle image velocimetry. *Measurement Science and Technology* **8**, 1406–1416.
- METTOT, CLEMENT, SIPP, DENIS & BEZARD, HERVE 2014 Quasi-laminar stability and sensitivity analyses for turbulent flows: Prediction of low-frequency unsteadiness and passive control. *Physics of Fluids* **26**, 045112.
- O’CONNOR, J. & LIEUWEN, T. 2011 Disturbance field characteristics of a transversely excited burner. *Combustion Science and Technology* **183**, 427–443.
- PARZANOVIC, VLADIMIR & CADOT, OLIVIER 2012 Experimental sensitivity analysis of the global properties of a two-dimensional turbulent wake. *Journal of Fluid Mechanics* **693**, 115–149.
- PERRIN, R., BRAZA, M., CID, E., CAZIN, S., BARTHET, A., SEVRAIN, A., MOCKETT, C. & THIELE, F. 2007 Obtaining phase averaged turbulence properties in the near wake of a circular cylinder at high reynolds number using pod. *Experiments in Fluids* **43**, 341–355.
- PETERS, N. 1999 The turbulent burning velocity for large-scale and small-scale turbulence. *Journal of Fluid Mechanics* **384**, 107–132.
- PIER, BENOT 2008 Local and global instabilities in the wake of a sphere. *Journal of Fluid Mechanics* **603**, 39–61.
- PIER, BENOIT & HUERRE, PATRICK 1996 Fully nonlinear global modes in spatially developing media. *Physica D* **97**, 206–222.
- POINSOT, T. J., TROUVE, A. C., VEYNANTE, D. P., CANDEL, S. M. & ESPOSITO, E. J. 1987 Vortex-driven acoustically coupled combustion instabilities. *Journal of Fluid Mechanics* **177**, 265–292.
- PRASAD, ANIL & WILLIAMSON, CHARLES H. K. 1997 The instability of the shear layer separating from a bluff body. *J. Fluid Mech.* **333**, 375–402.
- PROVANSAL, M., MATHIS, C. & BOYER, L. 1987 Bénard-von kármán instability: transient and forced regimes. *Journal of Fluid Mechanics* **182**, 1–22.
- REES, S. J. & JUNIPER, M. P. 2010 The effect of confinement on the stability of viscous planar jets and wakes. *Journal of Fluid Mechanics* **656**, 309–336.
- REYNOLDS, W. C. & HUSSAIN, A. K. M. F. 1972 The mechanics of an organized wave in turbulent shear flow. part 3. theoretical models and comparisons with experiments. *Journal of Fluid Mechanics* **54**, 263–288.
- ROSHKO, ANATOL 1954 On the development of turbulent wakes from vortex streets .
- SHANBHOUE, SANTOSH J., HUSAIN, S. & LIEUWEN, TIM 2009 Lean blowoff of bluff body stabilized flames: Scaling and dynamics. *Progress in Energy and Combustion Science* **35**, 98–120.

- SMITH, D. A. & ZUKOSKI, E. E. 1985 Combustion instability sustained by unsteady vortex combustion. In *AIAA/SAE/ASME/ASEE Joint Propulsion Conference*.
- SORIA, JULIO 1996 An investigation of the near wake of a circular cylinder using a video-based digital cross-correlation particle image velocimetry technique. *Experimental Thermal and Fluid Science* **12**, 221–233.
- SOTERIOU, M. C. & GHONIEM, A. F. 1994 The vorticity dynamics of an exothermic, spatially developing, forced reacting shear layer. *Proceedings of the Combustion Institute* **25**, 1265–1272.
- STRYKOWSKI, P. J. & SREENIVASAN, K. R. 1990 On the formation and suppression of vortex 'shedding' at low reynolds numbers. *J. Fluid Mech.* **218**, 71–107.
- STUART, J. T. 1958 On the non-linear mechanics of hydrodynamic stability. *Journal of Fluid Mechanics* **4**, 1–21.
- WILLERT, CHRISTIAN E. 1991 Digital particle image velocimetry. *Experiments in Fluids* **10**, 181–193.
- YU, MING-HUEI & MONKEWITZ, PETER A. 1990 The effect of nonuniform density on the absolute instability of two-dimensional inertial jets and wakes. *Phys. Fluids* **2**, 1175–1181.
- ZDRAVKOVICH, M. M. 1997 Flow around circular cylinders: A comprehensive guide through flow phenomena, experiments, applications, mathematical models, and computer simulations .
- ZINN, B. T. & LIEUWEN, T. 2005 In *Combustion Instabilities in Gas Turbine Engines: Operational Experience, Fundamental Mechanisms, and Modeling* (ed. T. Lieuwen & V. Yang), *Progress in Astronautics and Aeronautics*, vol. 210, pp. 3–24. American Institute of Aeronautics and Astronautics, Inc.